

A New “Offset” Analogue of the Classical Oxime-Bridged $[\text{Mn}^{\text{III}}_6]$ Single-Molecule Magnets

Katye M. Poole,[†] Maria Korabik,[‡] Muhandis Shiddiq,^{§,||} Kylie J. Mitchell,[†] Adeline Fournet,[†] Zhiliang You,[⊥] George Christou,[†] Stephen Hill,^{§,||} and Małgorzata Hołyńska^{*,†,⊥}

[†]Department of Chemistry, University of Florida, Gainesville, Florida 32611-7200, United States

[‡]Faculty of Chemistry, University of Wrocław, F. Joliot Curie 14, 50 383 Wrocław, Poland

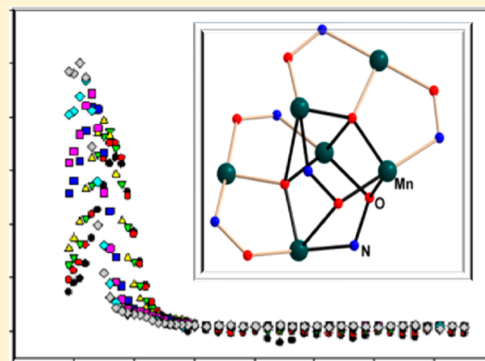
[§]Department of Physics, Florida State University, Tallahassee, Florida 32306, United States

^{||}National High Magnetic Field Laboratory, 1800 E. Paul Dirac Drive, Tallahassee, Florida 32310, United States

[⊥]Fachbereich Chemie and Wissenschaftliches Zentrum für Materialwissenschaften (WZMW), Philipps-Universität Marburg, Hans-Meerwein-Straße, D-35032 Marburg, Germany

Supporting Information

ABSTRACT: A new “offset” analogue of the classical $[\text{Mn}_6\text{O}_2]$ -core oxime-bridged single-molecule magnets is introduced with a modified stacking arrangement of the $[\text{Mn}_3\text{O}]$ units. Studies of the magnetic properties reveal antiferromagnetic exchange interactions, a spin $S = 4$ ground state and population of low-lying excited states. Slow relaxation of the magnetization can be detected, with a corresponding energy barrier of 35.8 K. Interpretation of these features is supported with high-frequency EPR studies, quantifying the easy-axis type magnetic anisotropy, leading to a biaxial system. Redox properties investigated by cyclic and differential pulse voltammetry reveal multiple irreversible redox processes.



1. INTRODUCTION

Oxime-bridged $[\text{Mn}_6\text{O}_2]$ -core complexes are an important and well-characterized group of compounds in terms of magneto-structural correlations.¹ Classical examples are the $[\text{Mn}^{\text{III}}_6\text{O}_2(\text{Et-sao})_6(\text{O}_2\text{CPh})_2(\text{EtOH})_4(\text{H}_2\text{O})_2]$ ^{2a} and $[\text{Mn}^{\text{III}}_6\text{O}_2(\text{Et-sao})_6(\text{O}_2\text{CPh}(\text{Me})_2)_2(\text{EtOH})_6]$ ^{2b} clusters following the “magic angle theory”.² In this theory, the dominant magnetic coupling within the $[\text{Mn}_6\text{O}_2]$ core is governed by the value of the torsion angle Mn–N–O–Mn. Over the “magic” value of $\sim 31^\circ$, ferromagnetic exchange is observed, which can be “switched” to antiferromagnetic for the lower torsion angle values. Since the discovery of this group of compounds, numerous modifications have been reported, mainly addressing the terminal part of the molecule.³ For instance, functional groups were introduced with supplementary organic ligands or the bridging salicylaldehyde ligands were substituted with bulky organic groups.³ Moreover, Brechin et al. introduced new structural types with a planar rod-like topology, where additional bridging ligands or mixed-valent $[\text{Mn}^{\text{III}}_4\text{Mn}^{\text{IV}}_2]$ cores are present and the magnetic properties behavior are different in comparison to the oxime-bridged $[\text{Mn}_6\text{O}_2]$ -core complexes.^{1a,b} In these compounds with $S = 6$ ground states and low-lying excited states, no single-molecule magnet (SMM) behavior was observed.

In this contribution, we report on an $[\text{Mn}^{\text{III}}_6]$ compound (**1**) with a novel modification of the $[\text{Mn}_6\text{O}_2]$ core, with 1-(1-

hydroxynaphthalen-2-yl)-ethanone oxime (*naphthsaoH*₂) acting as a ligand. Compound **1** ($[\text{Mn}_6\text{O}_2(\text{naphthsao})_6(\text{AcO})_2(\text{EtOH})(\text{H}_2\text{O})] \cdot x\text{EtOH} \cdot y\text{H}_2\text{O}$) shows SMM behavior.

We previously introduced the *naphthsaoH*₂ ligand and presented a series of its $[\text{Mn}_3]$ complexes.⁴ An $[\text{Mn}_9]$ defect supertetrahedron species, displaying enhanced energy barriers, was also constructed.⁵ A standard procedure developed by Brechin et al.¹ leads to an $[\text{Mn}_6]$ complex with a surprising new modification of the classical $[\text{Mn}_6\text{O}_2]$ core. When the reaction is carried out in methanol, the previously reported triangular $[\text{Mn}_3\text{O}(\text{naphthsao})_3(\text{CH}_3\text{OH})_5(\text{CH}_3\text{COO})]$ complex is isolated.⁴ The possibility of the related $[\text{Mn}_6\text{O}_2]$ analogue formation was already proved by Milios et al.⁶ An interesting compound with a novel modification was introduced, co-crystallizing with the classical core complex. No detailed magnetic property characterizations were reported due to the presence of the two molecular species in one crystal structure.

2. RESULTS AND DISCUSSION

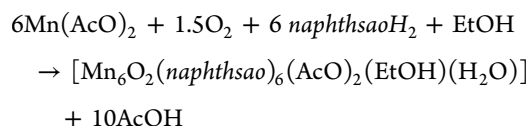
2.1. Synthesis. The title compound is isolated in a typical² procedure normally leading to the classical $[\text{Mn}_6\text{O}_2]$ -core compounds. In this procedure, the starting Mn(II) salt is

Received: November 20, 2014

Published: January 26, 2015

oxidized in ethanol solution under basic conditions induced by the addition of tetraethylammonium hydroxide to an Mn(III) complex stabilized by the bridging oxime ligands.

Reaction of manganese(II) acetate with equimolar amounts of *naphthsaoH*₂ ligand in EtOH resulted in a black solution, from which **1** was subsequently isolated in good yields (78%). Formation of **1** is summarized in the following equation



where atmospheric oxygen is assumed to be the oxidizing agent to generate Mn(III) from Mn(II), facilitated by the basic conditions provided by the addition of tetraethylammonium hydroxide. Formation of the new unexpected analogous structure is driven by the combination of the steric effect of the organic ligand and the ethanol molecules. Under similar conditions, exchange of the solvent to methanol leads to the well-known triangular [Mn₃] complexes⁴ and addition of potassium oxalate induces formation of a rare-topology [Mn₉] defect supertetrahedron complex.⁵

2.2. Structure and Redox Properties. The complex core contains two well-known oxime-bridged [Mn^{III}₃O] units, which are bound together in an unexpected way. Each triangular unit comprises three Mn³⁺ ions linked by the central μ₃-oxo ligand (with Mn–O bond lengths at 1.869(6)–1.924(7) and 1.874(5)–1.918(7) Å, respectively). The neighboring Mn³⁺ ions are joined by oxime groups of the *naphthsao* ligands (Figure 1c) lying at the edges of isosceles triangles. The Mn⋯Mn distances in these units are at 3.193(2)–3.266(3) and 3.176(4)–3.269(3) Å, respectively. In the classical example of an [Mn₆O₂] core,² the two [Mn₃O] units are antiparallel and joined through Mn–O_{oxime} bonds at one edge (Figure 1d). In **1**, these units are almost parallel and linked through two stronger Mn–O_{oxo/oxime} bonds, along with two weaker Mn–O_{oxime/oxo} bonds (Tables S2 and S3, Figures S1 and S3, Supporting Information; Figure 1a): Mn3–O25 at 2.272(7) Å, Mn5–O1 at 2.455(6) Å, Mn1⋯O2 at 2.787(6) Å, and Mn6⋯O23 at 2.550(7) Å, respectively. Thus, an unusual cage-like unit can be distinguished (Figure 1b) with stacking of tilted “Mn(O_{oxo})-(NO)_{oxime}Mn” rings. The “classical” and “offset” [Mn₆O₂] cores might be conveniently distinguished by the criterion of Mn⋯Mn distances, involving Mn atoms from different units. As expected, higher maximum distances are observed for the “classical core” compounds (see Table S4, Supporting Information). Similar considerations may lead to detection of other structural types within the [Mn₆O₂] family.

The complex molecules in **1** form columns extending along [001] (Figure S3) with no intermolecular interactions stronger than weak C–H⋯O and C–H⋯π contacts.

In order to assess the redox properties of **1** and its possible application as a precursor of mixed-valent products, its electrochemical behavior was studied in an MeCN solution in the presence of [nBu₄N][PF₆] (TBFP; 0.1 M) as a supporting electrolyte with the aid of cyclic and differential pulse voltammetry (CV and DPV) at 25 °C (Figure 2; Figures S5–S7, Supporting Information). As shown in Figure 2, the DPV of **1** exhibits two well-separated oxidation peaks in the potentials range of –0.17 to 1.30 V, with half-wave potential (E_{1/2}) at 0.52 and 0.98 V, respectively. These peaks correspond to the two vicinal peaks (p1 and p2) that are observed in the

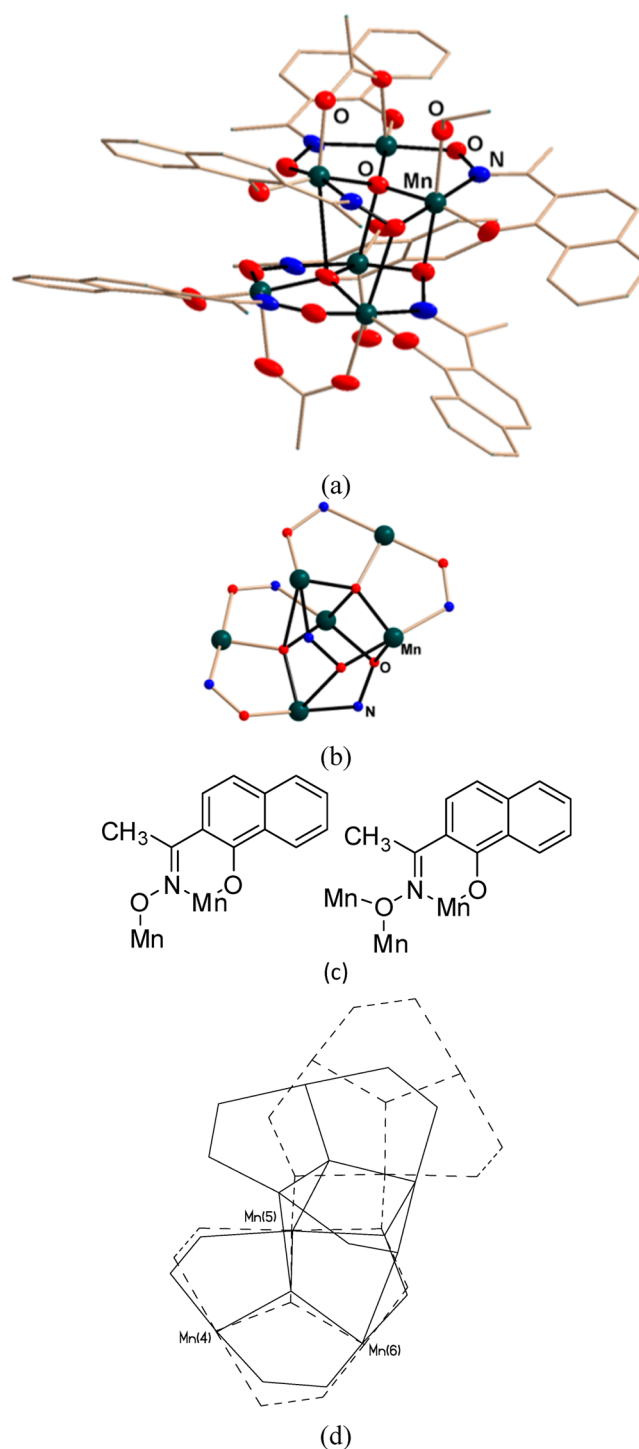


Figure 1. (a) Molecular structure of **1**. Thermal ellipsoids are plotted at the 20% probability level. (b) The complex core with a highlighted cage motif (see text). (c) The coordination modes of the organic ligand in **1**. (d) Overlap diagram for **1** (solid lines), and the “classical core” (dashed lines) example. Fitted atoms are labeled.

overall CV scan in the potential range of –2.20 to 2.30 V at a scan rate of 50 mV/s (Figure S5).

Electrochemical investigations of the related oxime-bridged polynuclear Mn^{III} complexes are scarce. An example is a tetranuclear [Mn^{II}₂Mn^{III}₂] complex with di-2-pyridyl ketone oxime as a ligand, displaying typical irreversible two oxidation and three reduction processes in its cyclic voltammogram.⁷ On

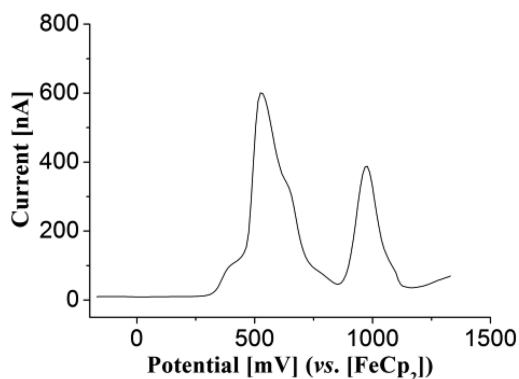


Figure 2. Differential pulse voltammogram, recorded at a platinum electrode in a MeCN solution of **1** (3 mM) in the presence of TBFP (0.1 M). Scan ranges and rates: -170 to 1300 mV, 10 mV/s; pulse amplitude of 50 mV.

the other hand, complexes with two Mn redox centers, for example, $[L'_2Mn^{III}_2(\mu-O)(\mu-CH_3CO_2)_2](ClO_4)_2 \cdot H_2O$ ($L' = N,N',N''$ -trimethyl-1,4,7-triazacyclononane), were comprehensively studied. This complex, also isolated as the hexafluorophosphate salt, exhibited a reversible one-electron wave at $E_{1/2} = 0.58$ V vs Fc^+/Fc (Fc —ferrocene), corresponding to the following process: $[Mn^{III}Mn^{III}] \rightarrow [Mn^{III}Mn^{IV}]$. CV measurements were performed under similar conditions as reported herein. Oxidation of the $[Mn^{III}Mn^{IV}]$ to $[Mn^{IV}_2]$ species could be observed at more positive potential values (>1.0 V vs Fc^+/Fc). However, the measurement was carried out in a more redox-inert solvent at lower temperature (liquid SO_2 , -40 °C).^{8–10} Thus, it can be stated that the two oxidation peaks obtained in the DPV experiment for **1** can be attributed to the single-electron Mn^{III}/Mn^{IV} couple oxidation processes. However, the oxidation processes involving the six Mn redox centers in **1** must be much more complicated, since the different intramolecular Mn··Mn distances within the complex molecule (see the previous paragraphs) most probably give rise to different magnitudes of interactions between the Mn redox centers through the bridging O atoms and/or through space. Consequently, the considerable separation between the two oxidation peaks in the DPV experiment ($\Delta E = 0.46$ V) indicates the presence of some strong interactions, while the shoulders on the first oxidation peaks could be considered a result of the weak interactions. Furthermore, a third oxidation peak overlapping with the oxidation of solvent and/or electrolyte could be observed, as the scan range of the DPV measurement was expanded to 2.30 V, revealing a possible complete oxidation of the six Mn^{III} redox centers with formation of the corresponding manganese(IV) products (Figure S5). In addition, the species corresponding to the two oxidation peaks in the potential range of -0.17 to 1.30 V in the DPV are unstable based on data from the successive CV measurements of **1** in the potential range of 0.03 – 1.30 V, at a scan rate of 50 mV/s, that exhibited a strong decrease in the intensity of the oxidation peaks from cycle to cycle (Figure S7a). This tendency persists also at higher scan rates and for small scan ranges (Figure S7b). The reason for this is probably the presence of water that reacts with the species, which is in accordance with the electrochemical investigations of the two previously mentioned binuclear Mn^{III} complexes,⁹ since the molecule of **1** contains water ligands that are difficult to remove completely.

2.2.1. Direct Current Magnetic Susceptibility Studies. Solid-state, variable-temperature *dc* magnetic susceptibility (χ_M) measurements were performed on samples of **1** in the 5.0 – 300 K range in a 0.1 T (1000 Oe) *dc* magnetic field. The results are shown as $\chi_M T$ vs T plots in Figure 3. Diamagnetic corrections were applied to the magnetic susceptibilities using Pascal's constants.¹¹

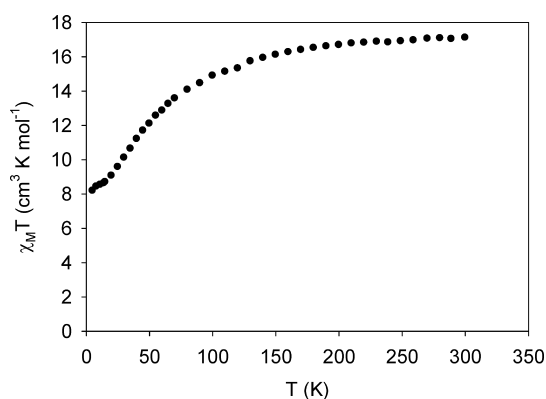


Figure 3. Plot of $\chi_M T$ vs T for complex **1**.

For complex **1**, $\chi_M T$ gradually decreases from 17.25 cm^3 K mol^{-1} at 300 K to a value of ~ 15 cm^3 K mol^{-1} at 100 K and then decreases rapidly to 8.25 cm^3 K mol^{-1} at 5.0 K (Figure 3). The 300 K value is slightly less than the spin-only ($g = 2$) value of 18 cm^3 K mol^{-1} for six noninteracting Mn^{III} ions. The decrease in $\chi_M T$ upon cooling is indicative of antiferromagnetic exchange interactions within the cluster. $\chi_M T$ appears to be heading for a final value of ~ 8 cm^3 K mol^{-1} at low temperature, corresponding to the spin-only ($g = 2$) value of a species with an $S = 4$ ground state.

To confirm the indicated $S = 4$ ground state for complex **1**, and to estimate the magnitude of the zero-field-splitting parameter, D , magnetization vs *dc* field measurements were made on restrained samples at applied magnetic fields and temperatures in the 0.1 – 7 T and 1.8 – 10.0 K ranges, respectively (Figure S8, Supporting Information). However, several attempts to fit the data assuming only the ground state is populated were not very successful, suggesting population of low-lying excited states.

2.2.2. Alternating Current Magnetic Susceptibility Studies. Solid-state, variable-temperature *ac* magnetic susceptibility (χ_M) measurements were performed on **1** in the 1.8 – 15 K range in a 3.5 G *ac* magnetic field; the results are shown in Figure 4. Diamagnetic corrections were applied to the magnetic susceptibilities using Pascal's constants.¹¹

Alternating current (*ac*) susceptibility studies are a powerful complement to *dc* studies for determining the ground spin state of a system, because they remove the complications that arise from having a significant *dc* field present. The obtained in-phase χ'_M signal for the vacuum-dried preparation of complex **1** is plotted as $\chi'_M T$ versus T in Figure 4a; the susceptibility decreases smoothly from 9.34 to 7.34 cm^3 K mol^{-1} upon cooling from 15 to 4 K, providing further indication for low-lying excited states. Extrapolation of the data in this temperature range to 0 K, to avoid effects due to anisotropy (blocking: see below) and weak intermolecular interactions, gives a value of ~ 7 cm^3 K mol^{-1} , which is consistent with the spin-only value for an $S = 4$ ground state (10 cm^3 K mol^{-1}). Below 4 K, there is a sharp decrease in the in-phase *ac*

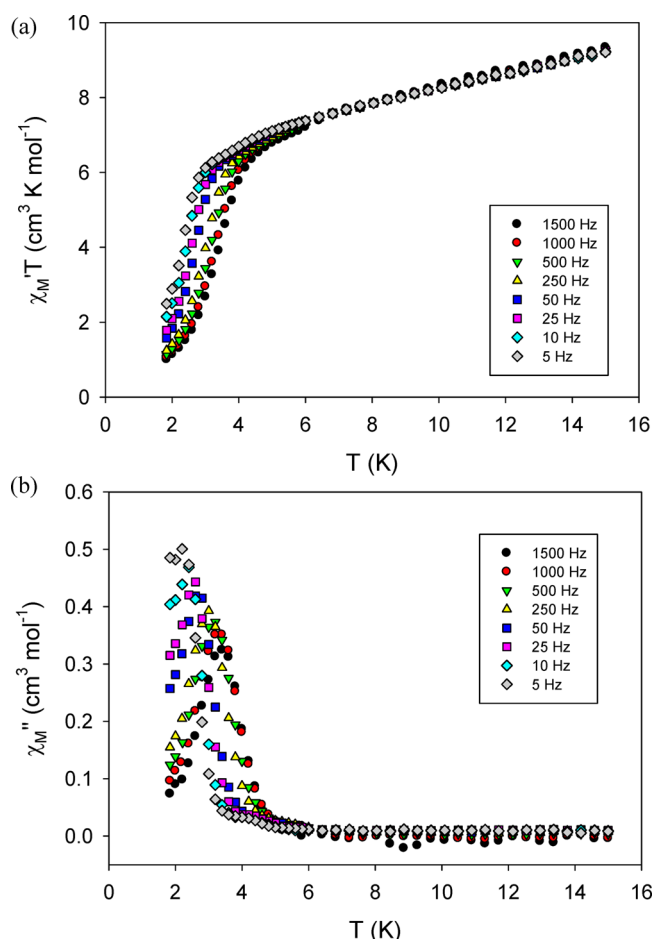


Figure 4. Alternating current magnetic susceptibility studies for **1**: in-phase plotted as $\chi_M' T$ (a) and out-of-phase plotted as χ_M'' (b).

susceptibility concomitant with an increase in the out-of-phase *ac* susceptibility (Figure 4). Both effects are frequency-dependent, which is consistent with SMM behavior. These measurements, therefore, suggest that **1** is an SMM with a significant barrier to magnetization relaxation.

The *ac* χ_M'' vs *T* plots can be used as a source of relaxation data for determining the effective energy barrier (U_{eff}) to magnetization relaxation, because the χ_M'' maximum occurs at a temperature below which the magnetization can no longer follow the *ac* driving field; i.e., the magnetization relaxation rate becomes too slow to keep up with the *ac* driving field. Therefore, at the temperature of the χ_M'' maximum, the relaxation rate ($1/\tau$, where τ is the relaxation time) is exactly equal to the angular driving frequency ($2\pi\nu$). Data obtained for **1** are displayed in Figure 5 in the form of a plot of the natural logarithm of the relaxation rate ($1/\tau$) versus $1/T_{\text{max}}$, where T_{max} corresponds to the χ_M'' maximum. According to the Arrhenius Law of eq 1, the data should lie on a straight line with a slope given by the effective barrier, U_{eff}

$$\tau^{-1} = \tau_0^{-1} \exp(-U_{\text{eff}}/kT) \quad (1)$$

where k is the Boltzmann constant and τ_0 is the pre-exponential factor. The fit of the data for **1** to eq 1 gave $U_{\text{eff}} = 35.8$ K and $\tau_0 = 2 \times 10^{-7} \text{ s}^{-1}$. *ac* susceptibility studies, therefore, confirm that **1** is an SMM.

An interesting comparison of U_{eff} and τ_0 can be made between complex **1** and other “classical” $[\text{Mn}_6\text{O}_2]$ -core

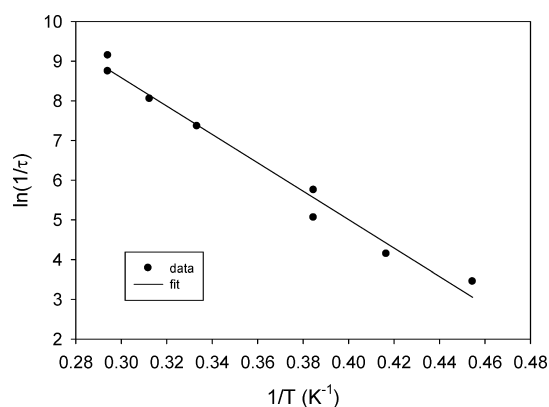


Figure 5. Arrhenius plot for sample of **1**. See text and eq 1 for fit parameters.

complexes in the systematic study of Brechin et al.^{1c} In the study, different spin ground states were investigated, extending from $S = 4$ to $S = 12$. For the $S = 4$ compounds, slightly lower τ_0/U_{eff} values of similar order as in **1** were observed ($2.0 \times 10^{-8} \text{ s}/28 \text{ K}$ and $6.8 \times 10^{-10} \text{ s}/31.7 \text{ K}$ for the two compounds, respectively). On the other hand, the energy barriers for the “classical” $S = 12$ compounds were as high as $\sim 86 \text{ K}$.

2.3. Electron Paramagnetic Resonance (EPR) Studies.

In order to more precisely quantify the magnetic anisotropy of **1**, we recorded high-field/high-frequency EPR spectra on a finely ground powder sample for a wide range of high frequencies from 50 to 450 GHz. Unlike single-crystal EPR spectra, powder measurements can provide information associated with all of the components of the magneto-anisotropy tensor in a single scan, with the main drawback being that a significant amount of sample is required ($>50 \text{ mg}$).¹² By performing measurements and spectral simulations at multiple frequencies, one can achieve tight constraints on the parameters associated with an effective giant-spin Hamiltonian, where fourth- (and higher-) order terms are often found to be significant for exchange-coupled clusters (particularly when there exist low-lying excited states).^{13,14} Figure 6a,c displays temperature-dependent, derivative mode (dI/dB) high-field EPR spectra recorded for **1** at 416 and 208 GHz, respectively; corresponding spectral simulations are displayed in Figure 6b,d. The fact that a strong peak-like feature is observed in Figure 6a at the lowest temperature, close to zero field, is indicative of a large zero-field gap ($>13 \text{ cm}^{-1}$) in the spectrum, i.e., strong magnetic anisotropy.

Derivative-mode powder EPR measurements typically give rise to features at the locations of the principal *x*-, *y*-, and *z*-components of the spectrum; for a more in-depth discussion, see ref 15. Therefore, a total of three resonances should be observed for a biaxial system as $T \rightarrow 0$, corresponding to each of the ground-state transitions for $B//x$, y , and z . However, in the present case, the field sweep range is insufficient to see all of these resonances in a single scan (*vide infra*), hence the importance of multifrequency measurements. Inspection of the lowest temperature data provides considerable insights into the anisotropy in **1**, even before simulations are performed. The 416 GHz spectrum exhibits a single peak below 1 T, corresponding to an onset of absorption far below the location of the isotropic $g = 2$ position (at $\sim 14.9 \text{ T}$ for 416 GHz), again providing a measure of the strong anisotropy in the system; no other resonances are seen over the entire field range. Several sharp features can be seen in the 208 GHz spectrum that

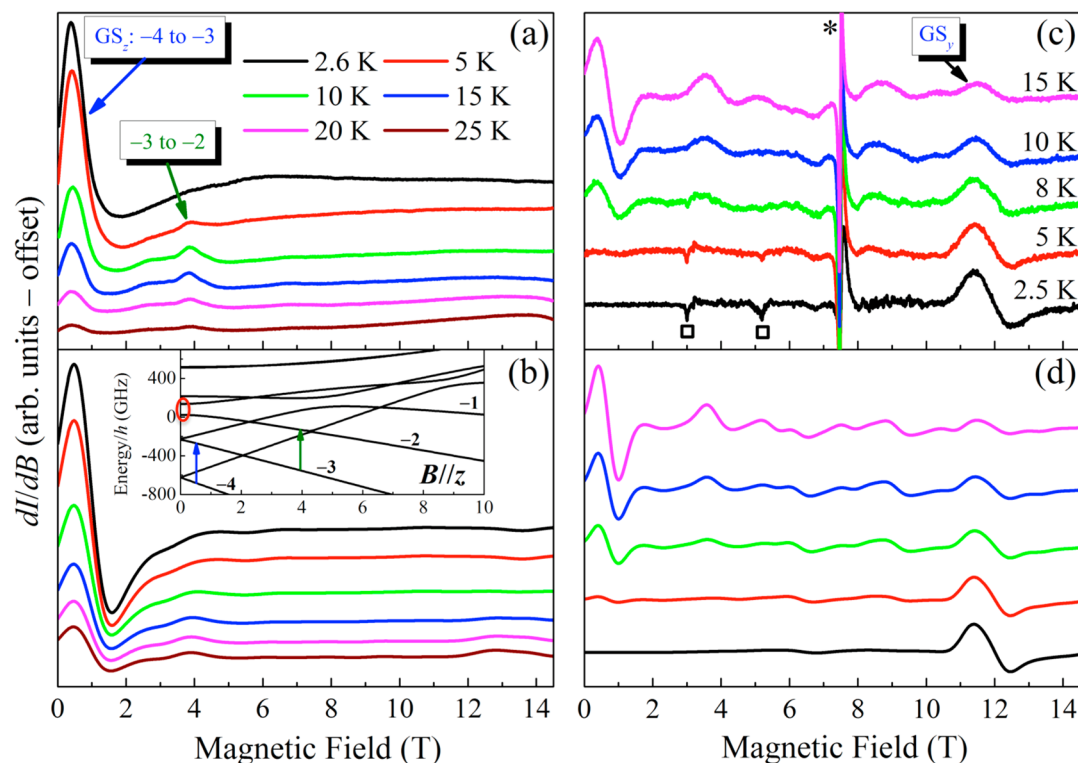


Figure 6. Temperature-dependent high-field powder EPR spectra for complex **1** [experimental (a, c) and simulated (b, d)], recorded in field derivative mode (dI/dB), at 416 GHz (a, b) and 208 GHz (c, d) in the temperature range from 2.5 to 25 K (see the Experimental Section for further details). The dips (labeled \square) at 3 and 5.2 T in (c) are attributed to paramagnetic oxygen impurities trapped in the KBr pellet, while the strong sharp large feature (*) observed at $g = 2$ (7.4 T) is attributed to paramagnetic impurities (Mn^{II}) in the sample holder. The broader features are attributed to **1**, and the ground-state transitions, GS_z and GS_y , have been labeled in (a) and (c), respectively; see main text for further explanation and details concerning the simulations. The inset in (b) depicts the Zeeman energy level diagram obtained via diagonalization of eq 2 for the easy-axis orientation ($B//z$). Some of the levels are labeled according to their approximate spin-projection (M_S), and two transitions have been indicated with vertical arrows that are color-coded to match the assignments in (a). The red oval highlights the appreciable zero-field tunneling gap between the $M_S = \pm 2$ states.

originate from known impurities: the dips labeled \square are due to oxygen trapped in the KBr pellet; and the strong feature labeled with an asterisk (*) at 7.4 T is attributed to $g = 2$ impurities (probably Mn^{II}) in the sample holder. The only other feature at the lowest temperature in Figure 6c occurs between 11 and 12.5 T; its line width suggests a similar origin to the low-field peak in Figure 6a. In the high-field limit, the first moment of the EPR spectrum should be located close to $g = 2$, such that two resonances occur above (below) $g = 2$ and one below (above) for an easy-axis (easy-plane) anisotropy. These considerations indicate an easy-axis-type anisotropy for **1**, albeit with a highly biaxial character. The low-field peak in Figure 6a corresponds to the parallel ($B//z$) ground-state resonance, GS_z , while the broad resonance in Figure 6c corresponds to one of the two perpendicular ground-state components, GS_y (i.e., $B//y$). Simulations (see below) show that the other perpendicular ground-state resonance, GS_x , lies beyond the maximum field range for all available frequencies. The biaxiality can be inferred on the basis of the positions of GS_z and GS_y relative to $g = 2$: GS_z is shifted ~ 14 T below $g = 2$, whereas GS_y is shifted only 4 T above $g = 2$. The ratio of these shifts should be closer to 2:1 for the uniaxial case. One can, in principle, make very crude estimates of the second-order axial and rhombic zero-field-splitting (zfs) parameters, D and E , respectively, from these very simple observations: by dividing the shift of GS_z from $g = 2$ by $[1.07 \times (2S + 1)] \text{ T/cm}^{-1}$, giving $D \sim -1.9 \text{ cm}^{-1}$ for $S = 4$, and by dividing the shift of GS_y from

the expectation for a uniaxial anisotropy (~ 7 T shift from $g = 2$) by the same quantity, giving $E \sim 0.4 \text{ cm}^{-1}$ for $S = 4$.

One can, of course, obtain far more precise estimates of the zfs parameters by performing simulations of the higher temperature spectra, which exhibit many more spectral peaks due to the thermal population of excited levels. We do so on the basis of the following effective giant-spin Hamiltonian:^{14,16}

$$\hat{H} = D\hat{S}_z^2 + E(\hat{S}_x^2 - \hat{S}_y^2) + B_4^0\hat{O}_4^0 + \mu_B\vec{B}\cdot\vec{g}\cdot\hat{S} \quad (2)$$

Here, \hat{S} is the spin operator, with components \hat{S}_i ($i = x, y, z$), \vec{B} is the applied magnetic field vector, \vec{g} is the Landé tensor, and μ_B the Bohr magneton; $\hat{O}_4^0 = 35\hat{S}_z^4 - 30\hat{S}_z^2(\hat{S} + 1)\hat{S}_z^2 + 25\hat{S}_z^2$ is the fourth-order axial zfs operator and B_4^0 the associated zfs parameter. The best simulations of the 416 and 208 GHz spectra are displayed in Figure 6b,d, respectively. The simulations assume a spin $S = 4$ ground state, in agreement with magnetic measurements, and the following spin Hamiltonian parameters: $D = -2.12 \text{ cm}^{-1}$, $|E| = 0.52 \text{ cm}^{-1}$, $B_4^0 = +4.67 \times 10^{-4} \text{ cm}^{-1}$, and $g_x = g_y = g_z = 2.00$. In order to reproduce the experimental line shapes/width, Gaussian distributions of both D and E were included in the simulations (FWHM of 0.02 cm^{-1} in each case). The inset to Figure 6b displays the corresponding energy level diagram for $B//z$, with resonance assignments for two of the peaks seen in the main panel. Labeling the resonances in Figure 6c,d is not straightforward, because most of the peaks belong to the

perpendicular spectrum ($B//x,y$) for which there is a strong mixing of spin sublevels due to the competing axial and transverse interactions; i.e., the high-field limit has not yet been reached. Overall, there is excellent agreement between the experimental and simulated spectra. Moreover, the obtained parametrization gives good agreement with measurements performed at other high frequencies (see Figure S9, Supporting Information).

The spectroscopic barrier to magnetization relaxation, $U_{\text{spec}} = |D|S^2 \approx 34 \text{ cm}^{-1}$ (or 49 K), can be estimated from the EPR parameters; full diagonalization of eq 2 gives $U_{\text{spec}} = 38 \text{ cm}^{-1}$, or $\sim 55 \text{ K}$ (see inset in Figure 6). These values are considerably higher than the effective barrier $U_{\text{eff}} = 35.8 \text{ K}$ determined from *ac* susceptibility studies of **1** prepared similarly to the EPR sample. However, the extreme biaxiality of **1** ($E/D \sim 0.25$, where 0.33 represents the most extreme case)¹⁴ gives rise to very significant under-barrier quantum tunneling, likely leading to a significant reduction of the effective relaxation barrier relative to the true barrier, U_{spec} .¹⁷ Indeed, as can be seen in the inset to Figure 6, there is an appreciable zero-field tunneling gap between the $M_S = \pm 2$ spin projection states (see red oval), suggesting that magnetization relaxation occurs via these levels. The center of mass of these two levels lies $\sim 34 \text{ K}$ above the $M_S = \pm 4$ ground state, which is in good agreement with the experimentally determined value of U_{eff} .

3. CONCLUSIONS

In conclusion, a new "offset" analogue of the classical oxime-bridged $[\text{Mn}_6\text{O}_2]$ -core complexes is introduced. The complex shows SMM behavior.

It could be expected that even more different forms of the classical $[\text{Mn}_6\text{O}_2]$ core may be synthesized, leading to unexplored magnetic properties and new insight into the magnetostructural correlations in this family of compounds. A careful design of the bridging oxime ligand should be the path to their successful isolation. Moreover, characterization of more complexes with a core related to **1** should enable a magnetostructural correlation to be developed in this class of compounds.

4. EXPERIMENTAL SECTION

4.1. Syntheses and Analyses Details. **4.1.1. General.** HPLC-grade absolute ethanol was used. 25% solution of tetraethylammonium hydroxide in methanol was stored under an Ar atmosphere prior to use. The organic ligand (1-(1-hydroxynaphthalen-2-yl)-ethanone oxime, *naphthsaoH*₂) was synthesized as reported elsewhere.⁴ Other chemicals (manganese(II) acetate tetrahydrate) were used as obtained commercially, without further purification.

4.1.2. Synthesis of $[\text{Mn}_6\text{O}_2(\text{naphthsao})_6(\text{AcO})_2(\text{EtOH})(\text{H}_2\text{O})] \cdot x\text{EtOH} \cdot y\text{H}_2\text{O}$ (1**).** 0.4 g (2 mmol) of 1-(1-hydroxynaphthalen-2-yl)-ethanone oxime (*naphthsaoH*₂) and 0.49 g (2 mmol) of manganese(II) acetate were combined in 50 mL of ethanol. To the resulting solution, 2 mL of tetraethylammonium hydroxide were added. The color of the mixture turned black. The mixture was stirred for 1 h, subsequently filtered and left for slow evaporation. Black crystals of **1** in the form of plates were obtained after 7–14 days at 78% yield.

Elemental analysis for sample dried under vacuum—analyzed as $\text{C}_{78}\text{H}_{68}\text{Mn}_6\text{N}_6\text{O}_{20} \cdot 3\text{H}_2\text{O}$ %Calcd (Found): C 51.95(51.57), H 4.70(4.27), N 4.66(4.01). IR bands (cm^{-1}): 382.06 (s), 391.66 (s), 422.07 (s), 443.55 (s), 481.23 (s), 521.89 (vs), 562.19 (s), 575.10 (s), 601.18 (s), 618.01 (vs), 636.44 (vs), 658.47 (vs), 736.57 (s), 795.32 (s), 897.31 (s), 991.17 (s), 1022.25 (s), 1034.13 (s), 1087.94 (m), 1136.47 (w), 1151.64 (w), 1209.79 (w), 1236.67 (w), 1251.50 (w), 1297.75 (w), 1345.92 (m), 1384.17 (s), 1419.64 (m), 1450.73 (w), 1516.79 (m), 1556.65 (m), 1618.98 (vw).

4.2. Physical Properties Measurements. Measurements of the magnetic properties were carried out on a Quantum Design MPMS XL SQUID magnetometer. The samples were dried under vacuum for 5 h and restrained in eicosane to prevent torquing.

Variable-temperature *dc* magnetic susceptibility measurements were performed in a 0.1 T field in the 5.0–300 K range. The susceptibility data were corrected with respect to the diamagnetic contribution of the holder and of the sample, as estimated from Pascal's constants.¹¹ Studies for the reduced magnetization plots were carried out at the applied fields of 1000, 5000, 10 000, 20 000, 30 000, 40 000, 50 000, 60 000, and 70 000 Oe.

The multifrequency EPR spectra on a powder sample of **1** were collected at the Electron Magnetic Resonance facility of the U.S. National High Magnetic Field Laboratory.¹² To avoid the field-induced alignment of the microcrystallites comprising the finely ground powder sample, it was pressed into a KBr pellet. Measurements were performed at variable frequencies from 50 to 438.4 GHz in the 2.5–25 K temperature range. The spectra were collected in derivative mode (dI/dB , where I represents the absorption intensity) using a transmission probe for which microwaves are propagated through cylindrical lightpipes.¹⁸ Variable-frequency microwaves were generated using a phase-locked Virginia Diodes solid-state source operating at a base frequency of $13 \pm 1 \text{ GHz}$, followed by a chain of multipliers and amplifiers. Microwave detection was provided by a helium-cooled bolometer. High magnetic fields of up to 14.5 T were generated using a superconducting magnet. Simulations of the EPR spectra and frequency-field plots were performed using the program EasySpin.¹⁶

All electrochemical measurements—cyclic and differential pulse voltammetry (CV and DPV)—were recorded under an Ar atmosphere at 25 °C, using 0.1 mol/L $[\text{nBu}_4\text{N}][\text{PF}_6]$ as the supporting electrolyte. The potentials were referenced internally to ferrocene, added at the end of the experiments. Working and counter electrodes: Pt; pulse amplitude for DPV: 50 mV.

Elemental analyses were performed on an Elementar Vario Micro cube (CHNS Mode) for samples dried under vacuum. IR spectra were recorded with the use of a Bruker Alpha-P Infrared-spectrometer equipped with a Platinum-ATR with a diamond crystal. Powder X-ray diffraction diffractograms were collected on a Bruker StadiVario device at 5–100° 2θ range using $\text{Cu K}\alpha$ radiation. The simulation of a theoretical pattern was carried out in Mercury software (Figure S4, Supporting Information).¹⁹ The thermogravimetric diagram was recorded for a 9.2 mg sample of **1** on a NETZSCH STA 409 CD device at a temperature range of 25–1200 °C and scanning rate of 5 K/min (Figure S2, Supporting Information). A three-step decomposition pattern was observed with first stages apparently corresponding to the release of interstitial solvent. X-ray diffraction data were collected at 100(2) K on a Stoe IPDS20 diffractometer equipped with an image plate detector and with graphite-monochromatized $\text{Mo K}\alpha$ radiation (see Table S1, Supporting Information, for the basic crystallographic data).

4.3. Details of Structure Refinement. The crystal structure was solved by direct methods in SHELXS97 and refined in SHELXL97 software.²¹ C-bonded H atoms were placed in their calculated positions with $U_{\text{eq}} = 1.2/1.5U_{\text{eq}}$ (parent C atom) for aromatic/methyl H atoms, respectively. SIMU/EADP restraints were used for displacement factors of some disordered atoms.

Extensive disorder of solvent molecules occupying structure voids had to be treated with the SQUEEZE procedure.²² The affected solvent occupied 32 voids, out of which the 8 largest were of about 705 Å³ in volume. In total, electron density corresponding to $\sim 70 \text{ e}^-$ asymmetric unit (7 water molecules or about 3 ethanol molecules) was thus removed.

Some difference Fourier maxima still present after further refinement cycles were interpreted as disordered water molecules: cooperatively disordered O1W/O2W (refined occupancies of 0.54(2)/0.46(2), respectively), O3W/O4W (refined occupancies of 0.61(2)/0.39(2), respectively), O5W/O6W (refined occupancies of 0.41(2)/0.59(3), respectively), and O7W, O8W with occupancies refined as free variables to 0.49(4), 0.33(3), respectively. On the final difference

Fourier map, the highest peak of $0.78 \text{ e}/\text{\AA}^3$ is located at 1.08 \AA from Mn5 atom.

CCDC-1029180 contains the supplementary crystallographic data for this paper. These data can be obtained free of charge from The Cambridge Crystallographic Data Centre via www.ccdc.cam.ac.uk/data_request/cif.

■ ASSOCIATED CONTENT

■ Supporting Information

Supplementary figures and tables for X-ray diffraction and TGA/CV analyses/magnetic properties. This material is available free of charge via the Internet at <http://pubs.acs.org>.

■ AUTHOR INFORMATION

Corresponding Author

*E-mail: holyńska@staff.uni-marburg.de (M.H.).

Author Contributions

M.H. performed syntheses and structural analyses. K.M.P., K.J.M., A.F., M.H., and G.C. performed magnetic measurements and their detailed analysis. Z.Y. and M.H. performed the cyclic voltammetry measurements and their analysis. M.S. and S.H. performed the HF-EPR experiments and their detailed analyses. All authors co-wrote the paper.

Notes

The authors declare no competing financial interest.

■ ACKNOWLEDGMENTS

M.H. gratefully acknowledges the help of Prof. Dr. S. Dehnen (generous support and helpful discussions), Dr. Polina Gavrilenko (Bruker GmbH) for powder X-ray diffraction data collection and DFG (project no. HO 5055/3-1)/NHMFL (project no. P07291) for funding. M.K. gratefully acknowledges financial support from the Polish National Science Centre (Grant no. NN204 198240). K.M.P. acknowledges the support of the National Science Foundation Graduate Research Fellowship under Grant No. DGE-0802270 and partial support from The National High Magnetic Field Laboratory, which is supported by NSF/DMR grant DMR-1157490 and the State of Florida. S.H. acknowledges the support of the NSF (DMR-1309463). G.C. acknowledges the support of the NSF (DMR-1213030).

■ REFERENCES

(1) (a) Milios, C. J.; Gass, I. A.; Vinslava, A.; Budd, L.; Parsons, S.; Wernsdorfer, W.; Perlepes, S. P.; Christou, G.; Brechin, E. K. *Inorg. Chem.* **2007**, *46*, 6215–6217. (b) Jones, L. F.; Inglis, R.; Cochrane, M. E.; Mason, K.; Collins, A.; Parsons, S.; Perlepes, S. P.; Brechin, E. K. *Dalton Trans.* **2008**, 6205–6210. (c) Milios, C. J.; Inglis, R.; Vinslava, A.; Bagai, R.; Wernsdorfer, W.; Parsons, S.; Perlepes, S. P.; Christou, G.; Brechin, E. K. *J. Am. Chem. Soc.* **2007**, *129*, 12505–12511. (d) Inglis, R.; Jones, L. F.; Milios, C. J.; Datta, S.; Collins, A.; Parsons, S.; Wernsdorfer, W.; Hill, S.; Perlepes, S. P.; Piligkos, S.; Brechin, E. K. *Dalton Trans.* **2009**, 3403–3412. (e) Milios, C. J.; Inglis, R.; Jones, L. F.; Prescimone, A.; Parsons, S.; Wernsdorfer, W.; Brechin, E. K. *Dalton Trans.* **2009**, 2812–2822. (f) Inglis, R.; Jones, L. F.; Milios, C. J.; Datta, S.; Collins, A.; Parsons, S.; Wernsdorfer, W.; Hill, S.; Perlepes, S. P.; Piligkos, S.; Brechin, E. K. *Dalton Trans.* **2009**, 3403–3412. (g) Accorsi, S.; Barra, A.-L.; Caneschi, A.; Chastanet, G.; Cornia, A.; Fabretti, A. C.; Gatteschi, D.; Mortalo, C.; Olivieri, E.; Parenti, F.; Rosa, P.; Sessoli, R.; Sorace, L.; Wernsdorfer, W.; Zobbi, L. *J. Am. Chem. Soc.* **2006**, *128*, 4742–4755. (h) Li, D.; Clérac, R.; Wang, G.; Yee, G. T.; Holmes, S. M. *Eur. J. Inorg. Chem.* **2007**, 1341–1346. (i) Stamatatos, T. C.; Abboud, K. A.; Wernsdorfer, W.; Christou, G. *Angew. Chem., Int. Ed.* **2007**, *46*, 884–888. (j) Ako, A. M.; Mereacre, V.; Clérac, R.; Wernsdorfer, W.; Hewitt, I. J.; Anson, C. E.; Powell, A.

Chem. Commun. **2009**, 544–546. (k) Cano, J.; Cauchy, T.; Ruiz, E.; Milios, C. J.; Stoumpos, C. C.; Stamatatos, T. C.; Perlepes, S. P.; Christou, G.; Brechin, E. K. *Dalton Trans.* **2008**, 234–240.

(2) (a) Milios, C. J.; Raptopoulou, C.; Terzis, A.; Lloret, F.; Vicente, R.; Perlepes, S. P.; Escuer, A. *Angew. Chem.* **2004**, *43*, 210–212. (b) Milios, C. J.; Vinslava, A.; Wernsdorfer, W.; Moggach, S.; Parsons, S.; Perlepes, S. P.; Christou, G.; Brechin, E. K. *J. Am. Chem. Soc.* **2007**, *129*, 2754–2755.

(3) Milios, C. J.; Kyritsis, P.; Raptopoulou, C. P.; Terzis, A.; Vicente, R.; Escuer, A.; Perlepes, S. P. *Dalton Trans.* **2005**, 501–511.

(4) Holyńska, M.; Frank, N.; Dehnen, S. Z. *Anorg. Allg. Chem.* **2012**, *638*, 2248–2251.

(5) Holyńska, M.; Frank, N.; Pichon, C.; Jeon, I.-R.; Clérac, R.; Dehnen, S. *Inorg. Chem.* **2013**, *52*, 7317–7319.

(6) Kozoni, C.; Manolopoulou, E.; Siczek, M.; Lis, T.; Brechin, E. K.; Milios, C. J. *Dalton Trans.* **2010**, 39, 7943–7950.

(7) Wiegardt, K.; Bossek, U.; Ventur, D.; Weiss, J. *J. Chem. Soc., Chem. Commun.* **1985**, 6, 347–349.

(8) Wiegardt, K.; Bossek, U.; Bonvoisin, J.; Beauvillain, P.; Girerd, J. J.; Nuber, B.; Weiss, J.; Heinze, J. *Angew. Chem., Int. Ed.* **1986**, *25*, 1030–1031.

(9) Wiegardt, K.; Bossek, U.; Nuber, B.; Weiss, J.; Bonvoisin, J.; Corbella, M.; Vitols, S. E.; Girerd, J. J. *J. Am. Chem. Soc.* **1988**, *110*, 7398–7411.

(10) (a) Jones, L. F.; Cochrane, M. E.; Koivisto, B. D.; Leigh, D. A.; Perlepes, S. P.; Wernsdorfer, W.; Brechin, E. K. *Inorg. Chim. Acta* **2008**, *361*, 3420–3426. (b) Prescimone, A.; Milios, C. J.; Sanchez-Benitez, J.; Kamenev, K. V.; Loose, C.; Kortus, J.; Moggach, S.; Murrie, M.; Warren, J. E.; Lennie, A. R.; Parsons, S.; Brechin, E. K. *Dalton Trans.* **2009**, 4858–4867. (c) Martinez-Lillo, J.; Chamoreau, L.-M.; Proust, A.; Verdager, M.; Gouzerh, P. C. R. *Chim.* **2012**, *15*, 889–894. (d) Martinez-Lillo, J.; Tomsa, A.-R.; Li, Y.; Chamoreau, L.-M.; Cremades, E.; Ruiz, E.; Barra, A.-L.; Proust, A.; Verdager, M.; Gouzerh, P. *Dalton Trans.* **2012**, 41, 13668–13681.

(11) Weast, R. C. *CRC Handbook of Chemistry and Physics*, 64th ed.; CRC Press: Boca Raton, FL, 1984.

(12) Baker, M. L.; Blundell, S. J.; Domingo, N.; Hill, S. *Struct. Bonding* **2014**, DOI: 10.1007/430_2014_155.

(13) Hill, S.; Datta, S.; Liu, J.; Inglis, R.; Milios, C. J.; Feng, P. L.; Henderson, J. J.; del Barco, E.; Brechin, E. K.; Hendrickson, D. N. *Dalton Trans.* **2010**, 39, 4693–4707.

(14) Liu, J.; del Barco, E.; Hill, S. A Microscopic and Spectroscopic View of Quantum Tunneling of the Magnetization. In *Molecular Magnets*; Bartolomé, J., Luis, F., Fernández, J. F., Eds.; Springer Series on NanoScience and Technology; Springer-Verlag: Berlin, 2014; pp 77–110.

(15) Houton, E.; Taylor, S.; Beedle, C. C.; Cano, J.; Piligkos, S.; Hill, S.; Ryder, A. G.; Brechin, E. K.; Jones, L. F. *Dalton Trans.* **2012**, 41, 8340–8347.

(16) Stoll, S.; Schweiger, A. *J. Magn. Reson.* **2006**, *178*, 42–55.

(17) Hill, S.; Murugesu, M.; Christou, G. *Phys. Rev.* **2009**, *B80*, 174416.

(18) Hassan, A. K.; Pardi, L. A.; Krzystek, J.; Sienkiewicz, A.; Goy, P.; Rohrer, M.; Brunel, L. C. *J. Magn. Reson.* **2000**, *142*, 300–312.

(19) *Mercury*, ver. 2.3; CCDC: Cambridge, U.K., 2001–2009.

(20) X-AREA (Version 1.54) and X-RED32 (Version 1.54); Stoe & Cie: Darmstadt, Germany, 2002.

(21) Sheldrick, G. M. *SHELXTL S.1*; Bruker AXS Inc.: Madison, WI, 1997.

(22) Spek, A. L. *Acta Crystallogr.* **2009**, *D65*, 148–155.